

Detecting single infrared photons with 93% system efficiency

F. Marsili^{1*}, V. B. Verma¹, J. A. Stern², S. Harrington¹, A. E. Lita¹, T. Gerrits¹, I. Vayshenker¹, B. Baek¹, M. D. Shaw², R. P. Mirin¹ and S. W. Nam^{1*}

Q1

1 Single-photon detectors¹ at near-infrared wavelengths with
2 high system detection efficiency (>90%), low dark count rate
3 (<1 c.p.s.), low timing jitter (<100 ps) and short reset time
4 (<100 ns) would enable landmark experiments in a variety of
5 fields^{2–6}. Although some of the existing approaches to single-
6 photon detection fulfil one or two of the above specifications¹,
7 to date, no detector has met all of the specifications simulta-
8 neously. Here, we report on a fibre-coupled single-photon
9 detection system that uses superconducting nanowire single-
10 photon detectors⁷ and closely approaches the ideal perform-
11 ance of single-photon detectors. Our detector system has a
12 system detection efficiency (including optical coupling losses)
13 greater than 90% in the wavelength range $\lambda =$
14 1,520–1,610 nm, with a device dark count rate (measured with
15 the device shielded from any background radiation) of ~ 1 c.p.s.,
16 timing jitter of ~ 150 ps FWHM and reset time of 40 ns.

17 Superconducting nanowire single-photon detectors (SNSPDs)^{7,8}
18 have outperformed other near-infrared single-photon detector tech-
19 nologies in terms of dark count rate, timing resolution and reset
20 time¹. However, after over ten years of research, the system detection
21 efficiency (SDE, which includes the efficiency of the optical coupling
22 to the detector) of SNSPDs has been limited to 36% at a wavelength
23 λ of 1,550 nm (ref. 9) because (i) the superconducting material used
24 (typically, polycrystalline NbN) has limited compatibility with the
25 structures that enhance the optical coupling and absorption of the
26 detectors, and (ii) the internal detection efficiency (the probability
27 that the absorption of one photon in a nanowire results in a
28 response pulse) of typical SNSPDs (based on 100-nm-wide NbN
29 nanowires) does not show saturation as a function of the bias
30 current I_B . The superconducting properties of NbN films depend
31 on the crystal phase of the films¹⁰ and are affected by crystal
32 defects^{11,12}, which limits (i) the fabrication yield of large-area
33 devices¹², (ii) the choice of substrates for fabrication and (iii) the
34 design parameters of optical structures that would enhance absorp-
35 tion in the nanowires. Furthermore, although 30- and 20-nm-wide
36 NbN nanowires have demonstrated saturated detection efficiency at
37 $\lambda = 1,550$ nm (ref. 13), the fabrication of large-area SNSPDs (which
38 allow efficient optical coupling) based on such narrow nanowires
39 remains challenging. We recently reported on the fabrication of
40 SNSPDs based on a different superconducting material, amorphous
41 tungsten silicide ($W_{0.75}Si_{0.25}$, or WSi)¹⁴. Because the crystal struc-
42 ture of WSi is homogeneously disordered, WSi superconducting
43 nanowires are more robust with respect to structural defects than
44 NbN nanowires (which allows the fabrication of larger-area
45 devices), can be deposited on a variety of substrates, allowing
46 more degrees of freedom in optimizing the optical coupling and
47 the absorption of the detectors. Furthermore, WSi SNSPDs based
48 on nanowires as wide as 150 nm have shown saturated SDE

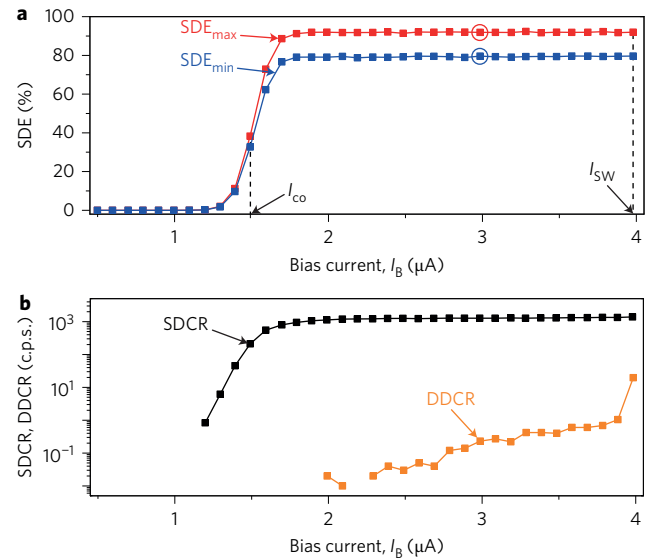


Figure 1 | Bias current dependence of SDE, SDCR and DDCR. a, SDE versus bias current I_B for two different polarizations of light at $\lambda = 1,550$ nm. The SNSPD used was based on 4.5-nm-thick, 120-nm-wide nanowires with a pitch of 200 nm. The SNSPD covered a square area with dimensions of $15 \mu m \times 15 \mu m$. The dashed lines indicate the cutoff current (I_{co} , which is defined as the bias current at the inflection point of the SDE versus I_B curve¹³) and the switching current (I_{sw} , which is defined as the maximum current the device could be biased at without switching to the normal, non-superconducting state) of the device. At $I_B = 3 \mu A$, the average and 1σ uncertainty of the maximum and minimum SDE were $SDE_{max} = 93.2 \pm 0.4\%$ (red circle) and $SDE_{min} = 80.5 \pm 0.4\%$ (blue circle) (see Supplementary Information). The experimental value of the SDE was lower than the design value of the absorption of the SNSPDs (>99%), which we attribute to several possible causes (see Supplementary Information): (i) our imperfect knowledge of the refractive index of the materials used in the optical stack; (ii) fabrication imperfections; (iii) coupling losses; and (iv) the non-unity internal detection efficiency of the SNSPDs. **b**, SDCR and DDCR versus I_B for the device in **a**. The SDE_{max} , SDE_{min} and SDCR curves were obtained at $T = 120$ mK by averaging six subsequent acquisitions of the curves. Error bars for each point are not plotted for clarity, but the uncertainty is described in the Supplementary Information.

Q2

Q2

Q2

versus I_B curves¹⁴ in the near-infrared, probably because the size
of the photon-induced perturbation of the superconducting
state^{15,16} is larger in WSi than in NbN. In earlier reported work¹⁴,
WSi SNSPDs only achieved $SDE \approx 20\%$ at $\lambda = 1,550$ nm because
the detectors were fabricated on bare oxidized silicon wafers and

53

¹National Institute of Standards and Technology, 325 Broadway, MC 815.04, Boulder, Colorado 80305, USA, ²Jet Propulsion Laboratory, California Institute of Technology, 4800 Oak Grove Drive, Pasadena, California 91109, USA. *e-mail: francesco.marsili@nist.gov; saewoo.nam@nist.gov

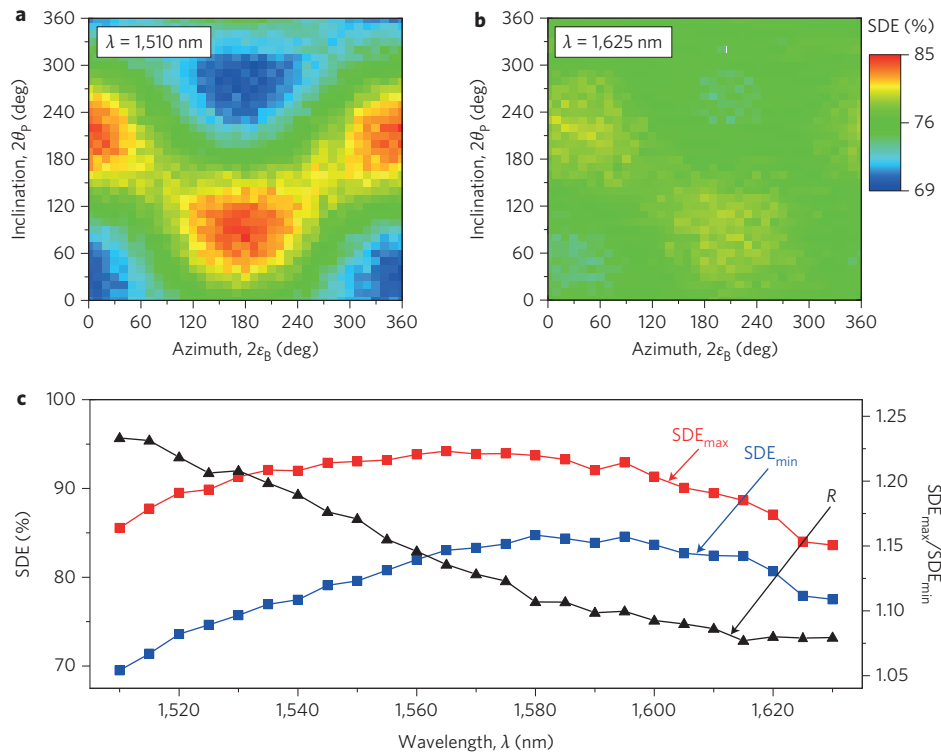


Figure 2 | Polarization and wavelength dependence of SDE. **a,b**, SDE (in colour scale) versus the inclination ($2\theta_p$) and azimuth ($2\epsilon_B$) angles of the polarization vector on the Poincaré sphere at $\lambda = 1,510$ nm (**a**) and $\lambda = 1,625$ nm (**b**). The ratio between maximum and minimum values of the SDE ($R = SDE_{max}/SDE_{min}$) varied from $R = 1.23$ at $\lambda = 1,510$ nm to $R = 1.08$ at $\lambda = 1,625$ nm because the wavelength dependence of the absorption of the optical stack was different for different polarizations^{23,24} (see Supplementary Information). **c**, Wavelength dependence of maximum SDE (SDE_{max}), minimum SDE (SDE_{min}) and ratio $R = SDE_{max}/SDE_{min}$. The measured parameters of the optical stack are, from top (illumination side) to bottom, 213-nm-thick TiO_2 , 231-nm-thick SiO_2 , 4.5-nm-thick, 120-nm-wide WSi nanowires with 200 nm pitch, 230-nm-thick SiO_2 , 80-nm-thick gold. The thickness of the WSi layer was estimated from the deposition time. The thicknesses of the TiO_2 and SiO_2 layers were estimated by white-light ellipsometry on reference samples from the deposition runs. The width and pitch of the nanowires were measured by scanning electron microscopy. Experimental SDE_{max} versus λ and SDE_{min} versus λ curves were obtained by averaging three subsequent acquisitions. The bias current was $I_B = 3.8$ μ A and the temperature was $T = 120$ mK.

1 were manually aligned to the optical fibre. Here, we report WSi
 2 SNSPDs embedded in an optical stack designed to enhance absorp-
 3 tion (see Supplementary Information) at $\lambda = 1,550$ nm and coupled
 4 to single-mode optical fibres at $\lambda = 1,550$ nm with a self-aligned
 5 mounting scheme based on silicon micromachining¹⁷. Using
 6 WSi SNSPDs, we constructed a detector system with SDE as
 7 high as $\sim 93\%$ around $\lambda = 1,550$ nm, a system dark count rate of
 8 $\sim 1 \times 10^3$ c.p.s. (primarily due to background radiation), a timing
 9 jitter of ~ 150 ps full-width at half-maximum (FWHM) and a
 10 reset time of 40 ns. The only other single-photon detector that
 11 has demonstrated SDE $> 90\%$ at $\lambda = 1,550$ nm is the transition-
 12 edge sensor (TES)¹⁸. However, the TES has orders of magnitude
 13 larger recovery time (~ 1 μ s) and timing jitter (the best value to
 14 date is ~ 5 ns; ref. 19) than WSi SNSPDs, and requires a complicated
 15 superconducting readout circuit.

16 We characterized our single-photon detection system by using 28
 17 different SNSPDs from five fabrication runs. We measured SDE $>$
 18 85% with 50% of the detectors tested so far (see Supplementary
 19 Information). Figure 1a shows the bias dependence of SDE (see
 20 Methods and Supplementary Information) for our best device. As
 21 the detection efficiency of SNSPDs varies with the polarization of
 22 the incident light²⁰, the polarization state of the light was varied
 23 on the Poincaré sphere to maximize or minimize the counts from
 24 the detector. We therefore obtained a maximum (SDE_{max} , red
 25 curve) and minimum (SDE_{min} , blue curve) SDE versus I_B curve.
 26 Both the SDE_{max} and SDE_{min} curves had a sigmoidal shape, and
 27 saturated at $SDE_{max} \approx 93\%$ and $SDE_{min} \approx 80\%$ for I_B values larger
 28 than a cutoff current $I_{co} = 1.5$ μ A and lower than the switching

29 current of the device, $I_{SW} = 4$ μ A. Figure 1b shows the bias depen-
 30 dence of the system dark count rate (SDCR, the response pulse
 31 count rate measured when the input fibre to the system is blocked
 32 by a shutter) and of the device dark count rate (DDCR, the response
 33 pulse count rate measured when the fibre is disconnected from the
 34 device inside the refrigerator). The SDCR versus I_B curve has a sig-
 35 moidal shape similar to the SDE versus I_B curves shown in Fig. 1a,
 36 and saturated at SDCR $\approx 1 \times 10^3$ c.p.s. for $I_B > I_{co}$. The DDCR was
 37 ≤ 1 c.p.s. for most of the bias range ($I_B \leq 0.97I_{SW}$), which is approxi-
 38 mately two orders of magnitude lower than the DDCR of NbN
 39 SNSPDs with a similar active area and fill factor²¹. We concluded
 40 that the SDCR is dominated by background photons.

41 Typically, the detection efficiency of SNSPDs varies significantly
 42 with the polarization of the incident light (by a factor of ~ 2 at
 43 $\lambda = 1,550$; refs 20,22). However, a detector with polarization-insensitive
 44 SDE would be desirable for many applications¹. We therefore
 45 characterized the polarization and wavelength dependence of the
 46 SDE by mapping the SDE onto the Poincaré sphere in the wave-
 47 length range $\lambda = 1,510$ – $1,630$ nm (we call these plots Poincaré
 48 maps of the SDE). Figure 2a,b shows the Poincaré maps at
 49 $\lambda = 1,510$ nm and $\lambda = 1,625$ nm. The positions of the maxima and
 50 minima of the Poincaré maps are approximately the same at
 51 the two wavelengths. However, the ratio between maximum and
 52 minimum values of the SDE ($R = SDE_{max}/SDE_{min}$) change with
 53 wavelength. Figure 2c shows the wavelength dependence of
 54 SDE_{max} (red squares), SDE_{min} (blue squares) and R (black triangles),
 55 which were obtained by extracting the maxima and minima of the
 56 Poincaré maps at each wavelength. Although the SDE of our

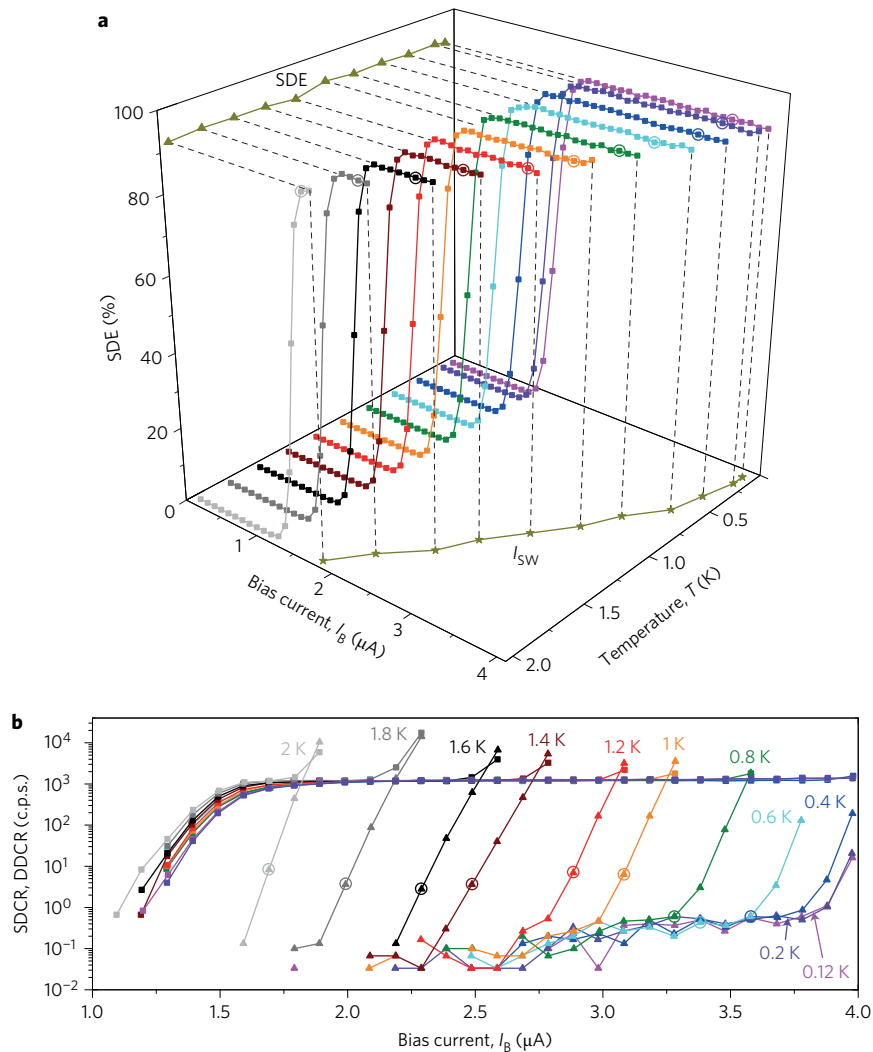


Figure 3 | Temperature dependence of SDE, SDCR and DDCR. **a**, SDE at $\lambda = 1,550$ nm versus bias current I_B and temperature T . Dark yellow curves on the I_B - T and SDE- T planes represent the temperature dependence of I_{SW} (stars) and SDE at $I_B = I_{SW}$ (triangles). Coloured circles indicate the data point at which $I_B \approx 0.9I_{SW}$ and SDE $\approx 90\%$ at each temperature. **b**, SDCR (squares) and DDCR (triangles) versus bias current I_B in the temperature range $T = 0.12$ - 2 K. Coloured circles indicate the data point at which $I_B \approx 0.9I_{SW}$ and DDCR < 10 c.p.s. at each temperature (the circles for $T = 0.4, 0.2$ and 0.12 K overlap). SDCR and DDCR curves were obtained by averaging three subsequent acquisitions of the curves. We did not observe any variation in I_{SW} between the different acquisitions of the curves.

Q6

1 detector showed a non-negligible polarization dependence, the
 2 results shown in Fig. 2c suggest that the optical stack could be
 3 designed to eliminate the polarization dependence of the SDE at a
 4 particular wavelength (which, however, may differ from the wave-
 5 length for the maximum SDE).

6 Most of the readily accessible closed-cycle refrigeration technol-
 7 ogies²⁵ do not reach a base temperature below 1 K. It would there-
 8 fore be desirable to operate our detector above 1 K without
 9 degrading its performance. As the critical temperature of our
 10 SNSPD was $T_C = 3.7$ K, we characterized the performance of the
 11 system as a function of temperature by measuring the bias
 12 dependence of SDE, SDCR and DDCR in the temperature range
 13 $T = 120$ mK- 2 K. As shown in Fig. 3a, although I_{SW} decreases
 14 and approaches I_{co} with increasing temperature (dark yellow stars
 15 on the I_B - T plane), the SDE versus I_B curve saturates to $\sim 93\%$
 16 over the whole temperature range $T = 120$ mK- 2 K (dark yellow tri-
 17 angles on the SDE- T plane). As shown in Fig. 3b, the DDCR at the
 18 switching current increases with temperature, from ~ 20 c.p.s. at
 19 $T = 120$ mK to $\sim 10 \times 10^3$ c.p.s. at $T = 2$ K, and is comparable to
 20 the SDCR for $T > 0.8$ K. Although the bias range for efficient,

low-dark-count-rate single-photon detection decreases with 21
 increasing temperature, the detector shows SDE $\approx 90\%$ and 22
 DDCR < 10 c.p.s. for $I_B \approx 0.9I_{SW}$ over the temperature range 23
 investigated (coloured circles in Fig. 3a,b), confirming that we could 24
 operate the detector system at relatively high cryogenic temperature 25
 without significantly degrading its sensitivity. 26

We characterized the timing performance of the detector system 27
 by measuring the histogram of the inter-arrival time^{13,26} of the 28
 response pulses and the timing jitter at $T = 120$ mK. Although in 29
 conventional NbN SNSPDs the decay time of the response pulse 30
 has been traditionally used as an estimate of the reset time of the 31
 detector²⁷, in our detector the reset time is significantly shorter 32
 than the decay time. As shown in Fig. 4a, the decay time of the 33
 response pulse of the SNSPD (τ) is $\tau \approx 120$ ns. However, Fig. 4b 34
 shows that the reset time of the detector (t_R) is as low as $t_R = 35$
 40 ns. The fact that t_R is a factor of ~ 3 lower than τ is due to the 36
 low I_{co} of the detector ($I_{co} \approx 0.4I_{SW}$; see Fig. 1a). Indeed, when 37
 the SNSPD switched back to the superconducting state after a hot 38
 spot nucleation event, it was sufficient that the current in the nano- 39
 wire increased above $\sim 0.4I_{SW}$ for the SDE to recover fully. Figure 4c 40

Q3

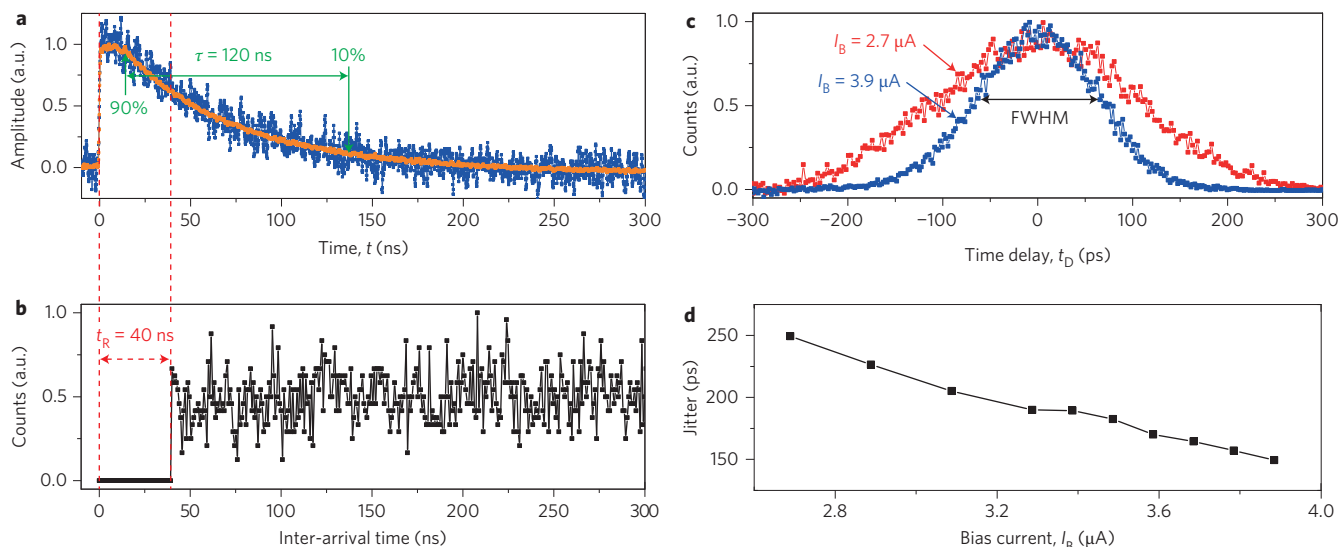


Figure 4 | Reset time and jitter. **a**, Single-shot (blue curve) and averaged (orange curve) oscilloscope traces of the response pulse of the SNSPD biased at $I_B = 3.8 \mu\text{A}$ ($I_B = 0.95I_{SW}$). The time t at which the curves reach 50% of the maximum of the average trace (158 mV) with positive slope was set to $t = 0$ s. The curves were normalized by the maximum of the average trace. The decay time of the SNSPD (τ) was defined as the time required for the pulse to decay from 90% to 10% of the maximum of the pulse (green arrows). **b**, Histogram of inter-arrival time (the period between two consecutive response pulses when the SNSPD is illuminated with a continuous-wave laser) of the SNSPD biased at $I_B = 3.8 \mu\text{A}$ ($I_B = 0.95I_{SW}$). The reset time (t_R) is defined as the period required for the histogram of the inter-arrival time to reach the first non-zero value. The histogram was normalized by its maximum value. **c**, IRF of the SNSPD biased at $I_B = 3.9$ (blue curve) and $I_B = 2.7 \mu\text{A}$ (red curve). The IRF at a particular I_B was obtained by calculating the histogram of the time delay t_D between the rising edge of the synchronization pulse of the laser and the rising edge of the response pulse of the SNSPD. Each IRF was normalized by its maximum value. The black arrow indicates the FWHM of the IRF acquired at $I_B = 3.9 \mu\text{A}$. **d**, Current dependence of the jitter of the detector system.

1 shows the instrument response function (IRF) of the detector system
 2 illuminated with a femtosecond-pulse laser for two different bias
 3 currents. The IRF becomes broader with decreasing I_B . Figure 4d
 4 shows the current dependence of the jitter of the detector system,
 5 which we define as the FWHM of the IRF. The system jitter
 6 decreases from 250 ps at $I_B = 0.67I_{SW}$ to 150 ps at $I_B = 0.97I_{SW}$.
 7 As the jitter increases with decreasing I_B and I_{SW} decreases with
 8 increasing temperature, operating the detector at higher temperature
 9 would result in a degradation of its timing resolution. The jitter of
 10 our detector system is higher than the values of 30–50 ps typically
 11 reported for conventional NbN SNSPDs⁸. However, the system
 12 jitter is dominated by the electrical noise of the readout circuit,
 13 rather than the intrinsic jitter of WSi SNSPDs (see Supplementary
 14 Information).

15 In conclusion, our single-photon detector system based on WSi
 16 SNSPDs demonstrated SDE $\approx 90\%$ at $\lambda = 1,550$ nm and DDCR $<$
 17 10 c.p.s. up to a temperature of $T = 2$ K. We expect our detector
 18 system to achieve a system dark count rate limited by the device
 19 intrinsic dark count rate (SDCR \approx DDCR $<$ 1 c.p.s.) by improving
 20 the filtering of the background photons. In the future, by adopting
 21 a parallel architecture (superconducting nanowire avalanche photo-
 22 detector, SNAP^{13,28,29}), we expect to reduce the reset time of our
 23 SNSPDs to $<$ 10 ns and to increase the signal-to-noise ratio¹³,
 24 which would allow the jitter of the detector system to be reduced.
 25 Finally, because of the relatively large bias range with saturated
 26 detection efficiency at $\lambda = 1,550$ nm, WSi SNSPDs have the poten-
 27 tial for high fabrication yield across a silicon wafer and broad wave-
 28 length sensitivity^{14,30}. These two features will enable two major
 29 advancements in the near future: (i) high SDE in the mid-infrared
 30 wavelength range, and (ii) large SNSPD arrays with near-unity
 31 efficiency from the visible to the mid-infrared spectral regions.

32 Methods

33 **Detector system and measurement setup.** The experimental setup used for the
 34 optical characterization of our detector system is presented in the Supplementary

Information. For the SDE and inter-arrival time measurements, we illuminated
 the detector using a fibre-coupled continuous-wave tunable laser with tuning range
 $\lambda = 1,510$ – $1,630$ nm. For jitter measurements, we used a mode-locked fibre laser
 with emission around 1,560 nm, pulse width of $<$ 100 fs and repetition rate of
 ~ 35 MHz. We controlled the polarization of the light from the lasers with a
 polarization controller. The light was then coupled to three variable optical
 attenuators (with nominal attenuation A_1 , A_2 and A_3) and to a micro-electro-
 mechanical system optical switch. The optical switch diverted the light at its input to
 the detector system (we call this output the detector port) or to a calibrated
 (see Supplementary Information) optical InGaAs power meter (we call this output
 the control port).

After fabrication, a device could be removed from the wafer¹⁷ and mounted
 inside a zirconia sleeve with an optical fibre. Holding both the detector chip and
 the optical fibre, the zirconia sleeve realized an optical alignment with a typical
 accuracy of $\pm 3 \mu\text{m}$ (ref. 17). All of the optical fibres used were silica C-band
 single-mode fibres. The optical fibre coupled to the detector inside the cryostat
 (a cryogen-free adiabatic demagnetization refrigerator) was coated with a
 multi-dielectric-layer anti-reflection coating that reduced the reflectivity ρ at the
 interface between the silica and the air (or vacuum) below 0.3% in the wavelength
 range of interest. The fibre coupled to the detector was then spliced to a fibre
 inside the cryostat. That cryostat fibre was fed out of the cryostat through a vacuum
 feed-through and then spliced to a fibre coupled to the detector port of the
 optical switch.

The detectors were wire-bonded to launching pads connected by SMP
 connectors to brass coaxial cables (2 GHz electrical bandwidth at 300 K). The
 devices were current-biased with a low-noise voltage source in series with a
 10 k Ω resistor through the d.c. port of a room-temperature bias-tee (40 dB isolation,
 100 kHz–4.2 GHz bandwidth on the radiofrequency port). The readout circuit
 consisted of a chain of two low-noise, room-temperature amplifiers
 (100 kHz–500 MHz bandwidth, 24 dB gain, 2.9 dB noise figure) connected to the
 radiofrequency port of the bias-tee. The amplified signal was connected to a
 225 MHz bandwidth counter (for detection efficiency measurements) or to an
 8 GHz bandwidth, 20 Gsample/s oscilloscope (for jitter and inter-arrival
 time measurements).

Estimation of SDE. The SDE was measured as the ratio of the photoresponse
 count rate (PCR) and the number of photons in the SNSPD fibre (N_{ph}), where
 $\text{SDE} = \text{PCR}/N_{ph}$. PCR was estimated as the difference between the response-pulse
 count rate (CR), measured with the laser beam attenuated ~ 80 dB ($A_2 = A_3 =$
 40 dB) and coupled to the detector, and the SDCR. We defined the SDCR as the
 response pulse count rate measured with the laser beam blocked by the shutters
 of the variable optical attenuators. N_{ph} at a particular wavelength λ was calculated

1 by using an estimate of the optical power in the SNSPD fibre (P_{SNSPD}) and the
 2 energy of a single photon at that wavelength.
 3 The SDE was measured at a particular wavelength with the following procedure.
 4 (i) We measured the splitting ratio of the optical switch (R_{SW}), which we defined as
 5 the ratio between the power at the detector and control ports of the switch. (ii) We
 6 then measured the real attenuation of attenuator 2,3 ($\alpha_{2,3}$) when the nominal
 7 attenuation of attenuator 2,3 was set to 40 dB ($A_1 = A_{3,2} = 0$ dB and $A_{2,3} = 40$ dB).
 8 (iii) With the attenuation of attenuator 2,3 set to zero ($A_2 = A_3 = 0$ dB), we varied
 9 the attenuation of attenuator 1 (A_1) to obtain the desired input optical power in the
 10 control port (P_C). (iv) We then closed the shutters of the three attenuators and
 11 measured the SDCR versus I_B curve. (v) We opened the shutters of the three
 12 attenuators, set the attenuation of attenuator 2 and 3 to 40 dB ($A_2 = A_3 = 40$ dB) to
 13 reduce the optical power to the single-photon level ($\sim 50 \times 10^3$ photons per second),
 14 and measured the CR versus I_B curve. We calculated the optical power in the
 15 SNSPD fibre as $P_{\text{SNSPD}} = P_C \cdot \alpha_2 \cdot \alpha_3 \cdot R_{\text{SW}} / (1 - \rho)$. Further details are presented in
 16 the Supplementary Information.

17 Received 2 August 2012; accepted 9 January 2013;
 18 published online XX XX 2013

19 References

- 20 1. Eisaman, M. D., Fan, J., Migdall, A. & Polyakov, S. V. Invited Review Article:
 21 Single-photon sources and detectors. *Rev. Sci. Instrum.* **82**, 071101 (2011).
- 22 2. Garg, A. & Mermin, N. D. Detector inefficiencies in the Einstein-Podolsky-
 23 Rosen experiment. *Phys. Rev. D* **35**, 3831–3835 (1987).
- 24 3. Ladd, T. D. *et al.* Quantum computers. *Nature* **464**, 45–53 (2010).
- 25 4. Gisin, N. & Thew, R. Quantum communication. *Nature Photon.* **1**,
 26 165–171 (2007).
- 27 5. Li, D. D. U. *et al.* Video-rate fluorescence lifetime imaging camera with CMOS
 28 single-photon avalanche diode arrays and high-speed imaging algorithm.
 29 *J. Biomed. Opt.* **16**, 096012 (2011).
- 30 6. Weibring, P., Edner, H. & Svanberg, S. Versatile mobile lidar system for
 31 environmental monitoring. *Appl. Opt.* **42**, 3583–3594 (2003).
- 32 7. Gol'tsman, G. N. *et al.* Picosecond superconducting single-photon optical
 33 detector. *Appl. Phys. Lett.* **79**, 705–707 (2001).
- 34 8. Natarajan, C. M., Tanner, M. G. & Hadfield, R. H. Superconducting nanowire
 35 single-photon detectors: physics and applications. *Supercond. Sci. Technol.*
 36 **25**, 063001 (2012).
- 37 9. Correa, R. E. *et al.* Single photon counting from individual nanocrystals in the
 38 infrared. *Nano Lett.* **12**, 2953–2958 (2012).
- 39 10. Toth, L. E. *Transition Metal Carbides and Nitrides* Ch. 7 (Academic Press, 1971).
- 40 11. Gaggero, A. *et al.* Nanowire superconducting single-photon detectors on
 41 GaAs for integrated quantum photonic applications. *Appl. Phys. Lett.* **97**,
 42 151108 (2010).
- 43 12. Marsili, F. *et al.* High quality superconducting NbN thin films on GaAs.
 44 *Supercond. Sci. Technol.* **22**, 095013 (2009).
- 45 13. Marsili, F. *et al.* Single-photon detectors based on ultra-narrow superconducting
 46 nanowires. *Nano Lett.* **11**, 2048–2053 (2011).
- 47 14. Baek, B., Lita, A. E., Verma, V. & Nam, S. W. Superconducting $a\text{-W}_x\text{Si}_{1-x}$
 48 nanowire single-photon detector with saturated internal quantum efficiency
 49 from visible to 1850 nm. *Appl. Phys. Lett.* **98**, 251105 (2011).
- 50 15. Semenov, A. D., Gol'tsman, G. N. & Korneev, A. A. Quantum detection by
 51 current carrying superconducting film. *Physica C* **351**, 349–356 (2001).
- 52 16. Bulaevskii, L. N., Graf, M. J. & Kogan, V. G. Vortex-assisted photon counts and
 53 their magnetic field dependence in single-photon superconducting detectors.
 164 *Phys. Rev. B* **85**, 014505 (2012).

17. Miller, A. J. *et al.* Compact cryogenic self-aligning fiber-to-detector coupling
 with losses below one percent. *Opt. Express* **19**, 9102–9110 (2011). 55
18. Lita, A. E., Miller, A. J. & Nam, S. W. Counting near-infrared single-photons
 with 95% efficiency. *Opt. Express* **16**, 3032–3040 (2008). 56
19. Lamas-Linares, A. *et al.* in *Proceedings of the Quantum Electronics and Laser*
Science Conference QTu3E.1 (Optical Society of America, 2012). 57
20. Anant, V. *et al.* Optical properties of superconducting nanowire single-photon
 detectors. *Opt. Express* **16**, 10750–10761 (2008). 58
21. Yamashita, T. *et al.* Origin of intrinsic dark count in superconducting nanowire
 single-photon detectors. *Appl. Phys. Lett.* **99**, 161105 (2011). 59
22. Dorenbos, S. N. *et al.* Superconducting single photon detectors with minimized
 polarization dependence. *Appl. Phys. Lett.* **93**, 161102 (2008). 60
23. Semenov, A. *et al.* Optical and transport properties of ultrathin NbN films and
 nanostructures. *Phys. Rev. B* **80**, 054510 (2009). 61
24. Driessen, E. F. C. *et al.* Impedance model for the polarization-dependent optical
 absorption of superconducting single-photon detectors. *Eur. Phys. J. Appl. Phys.*
47, 10701 (2009). 62
25. Ekin, J. W. *Experimental Techniques for Low-Temperature Measurements:*
Cryostat Design, Material Properties, and Superconductor Critical-Current
Testing (Oxford Univ. Press, 2007). 63
26. Stern, J. A. & Farr, W. H. Fabrication and characterization of superconducting
 NbN nanowire single photon detectors. *IEEE Trans. Appl. Supercond.* **17**,
 306–309 (2007). 64
27. Kerman, A. J. *et al.* Kinetic-inductance-limited reset time of superconducting
 nanowire photon counters. *Appl. Phys. Lett.* **88**, 111116 (2006). 65
28. Ejrnaes, M. *et al.* A cascade switching superconducting single photon detector.
Appl. Phys. Lett. **91**, 262509 (2007). 66
29. Marsili, F., Najafi, F., Dauler, E., Molnar, R. J. & Berggren, K. K. Afterpulsing and
 instability in superconducting nanowire avalanche photodetectors. *Appl. Phys.*
Lett. **100**, 112601 (2012). 67
30. Marsili, F. *et al.* Efficient single photon detection from 500 nanometer to
 5 micron wavelength. *Nanolett.* **12**, 4799–4804 (2012). 68

Acknowledgements

The authors thank R. M. Briggs, S. D. Dyer, W. H. Farr, J. Gao, M. Green, E. Grossman,
 P. D. Hale, R. W. Leonhardt, I. Levin and R. E. Muller for technical support, and S. Bradley,
 B. Calkins, A. Migdall and M. Stevens for scientific discussions. Part of this work was
 supported by the Defense Advanced Research Projects Agency (Information in a Photon
 programme). Part of this research was carried out at the Jet Propulsion Laboratory,
 California Institute of Technology, under a contract with the National Aeronautics and
 Space Administration.

Author contributions

F.M., V.B.V., J.A.S., A.E.L., B.B., R.P.M. and S.N. conceived and designed the experiments.
 F.M., V.B.V., J.A.S., S.H. and T.G. performed the experiments. F.M. and S.H. analysed
 the data. J.A.S., I.V., M.D.S. and S.N. contributed materials/analysis tools. F.M. wrote
 the paper.

Additional information

Supplementary information is available in the online version of the paper. Reprints and
 permission information is available online at <http://www.nature.com/reprints>. Correspondence
 and requests for materials should be addressed to F.M. and S.W.N.

Competing financial interests

The authors declare no competing financial interests.

Publisher: Nature

Journal: Nature Photonics

Article number: nphoton.2013.13

Author (s): Marsili *et al.*

Title of paper: Detecting single infrared photons with 93% system efficiency

Query no.	Query	Response
1	Two correspondence authors were mentioned at different points in the manuscript. We have included both – please confirm that both are to be retained, or indicate which is to be deleted.	
2	Can we be more specific about where you mean in the Supplementary Information? Section numbered or heading perhaps?	
3	I have changed the unit style here to conform to journal style. Please check that this is accurate as rearranged	
4	Please expand SMP for first use	
5	Ref 25 – please confirm that you intend to cite the entire book, or provide chapter number/page range, and chapter authors if appropriate	
6	By “subsequent” do you mean “consecutive”?	